






PREPARATION AND CHARACTERIZATION OF BIOCHAR-IRON OXIDE-PALYGORSKITE COMPOSITES FOR URANIUM(VI) REMOVAL FROM AQUEOUS SOLUTIONS

Ihor Pylypenko ^{a,b,*}, Iryna Kovalchuk ^{a,b}, Mykola Tsyba ^b, Yurii Lytvynenko ^c,
Oleksandr Shyrokov ^d

^a National Technical University of Ukraine "Igor Sikorsky Kyiv Polytechnic Institute",
37, Beresteyskiy ave., Kyiv, 03056, Ukraine

^b Institute for Sorption and Problems of Endoecology of NAS of Ukraine,
13, Oleha Mudraka str., Kyiv, 03164, Ukraine

^c Semenenko Institute of Geochemistry, Mineralogy and Ore Formation of NAS of Ukraine,
34, Palladina ave., Kyiv, 03142, Ukraine

^d Frantsevich Institute for Problems of Materials Science of NAS of Ukraine,
3, Omelyana Prytsaka str., Kyiv, 03142, Ukraine

*e-mail: i.pylypenko@kpi.ua

Abstract. This paper details the synthesis of palygorskite/biochar/iron oxide composites and their utilization for the remediation of water solutions contaminated with uranium(VI). The synthesis procedure involved the combination of iron chloride, starch, and palygorskite with subsequent pH adjustment, drying of the formed precipitate, and pyrolysis at 600°C. The synthesis of mesoporous materials, primarily composed of iron oxides, including magnetite and hematite, was confirmed using various characterization techniques, including FTIR, SEM, and XRD. It was shown that the adsorption of uranium(VI) reached a maximum of 100.2 µmol/g, exhibiting the highest affinity, which is associated with significant magnetite involvement, which facilitates the reduction processes of uranium(VI) to uranium(IV). The findings demonstrated that the uranium removal process was enhanced by a rise in pH, with significant adsorption and possible precipitation occurring under neutral conditions, so using these composite materials is suitable for in situ remediation of water solutions contaminated by uranium(VI).

Keywords: biochar composite, palygorskite, pyrolysis, adsorption, uranium(VI).

Received: 03 March 2025/ Revised final: 3 June 2025/ Accepted: 5 June 2025

Introduction

Environmental pollution with uranium(VI) is a serious problem that requires immediate attention. Hexavalent uranium is one of the most toxic radioactive substances, capable of causing severe diseases, including DNA mutations, kidney failure, and cancer [1]. Its compounds are highly soluble in water, especially stable anionic carbonate- and hydroxocomplexes, such as $[\text{UO}_2(\text{CO}_3)_3]^{4-}$ or $[\text{UO}_2(\text{OH})_2]^{2-}$, which can migrate long distances and accumulate in natural water systems. The inability of these anionic uranium(VI) species to undergo precipitation, unlike many metal cations, significantly limits their natural attenuation, thereby impeding self-purification processes and requiring the implementation of efficient removal techniques [2].

Heavy metal removal techniques like coagulation, ion exchange, precipitation, and

electrochemical processes aren't always effective at getting rid of U(VI) because its anionic complexes are very stable in water [3,4]. Moreover, these methods are often energy-intensive, require high maintenance costs, and lead to secondary contamination. Therefore, research into new materials capable of effectively binding and removing U(VI) from aqueous solutions is an important direction in environmental protection and eco-technologies.

The range of modern adsorption materials that can purify aqueous environments from heavy metals and radionuclides has significantly expanded due to recent scientific advances. Composites based on biochar [4], clay minerals [5], or metal oxides like iron oxides [6] are receiving particular attention. Biochar, synthesized through pyrolysis of organic raw materials, is a stable and environmentally safe material with a high specific surface area and chemical activity.

When it mixes with iron oxides or clays like palygorskite, it makes it easier to bind different kinds of U(VI) because there are more active sites on the surface [4].

Research by Li, M. *et al.* demonstrated the effectiveness of magnetic biochar-iron oxide composites for uranium(VI) removal from water up to 52.63 mg/g at pH 4.0 [7].

In the study [8], biochar-montmorillonite composites were successfully synthesized using a one-stage pyrolysis method in an oxygen-limited atmosphere. Oxytetracycline adsorption tests showed that the composites could hold 58.85 mg/g of oxytetracycline, 2.63 times more than the original biochar.

Tang, J. *et al.* developed a cost-effective attapulgite/carbon (APT/C) composite for wastewater treatment, using waste oil as a carbon source [9]. The material synthesis was carried out through a simple one-step calcination process. The composite showed high adsorption capacities of up to 215.8 mg/g for methyl violet and 256.5 mg/g for tetracycline.

Furthermore, composite materials based on biochar and clays show high stability across different pH levels, allowing their effective use in natural and industrial conditions where environmental parameters can vary significantly [10].

Sun, S. *et al.* demonstrated that iron oxide-modified biochar/attapulgite composites (Fe-BC/A) synthesized through a one-step pyrolysis process [11]. They show high efficiency in removing Cr(VI) from aqueous solutions. The maximum established adsorption capacity was 107 mg/g at pH 2.0 (for Fe-BC/A), which is twice the adsorption of the primary biochar (BC: 54.4 mg/g).

Using clay minerals, biomass, and iron compounds as raw materials allows the production of composites with increased specific surface area and developed porosity. For instance, a study [12] demonstrated the production of iron-clay biochar through the pyrolysis of bamboo biomass mixtures that had been pre-treated with iron-sulphate-clay suspensions.

The studies reviewed above confirm that such composites can effectively remove U(VI) and other pollutants from water at pH 4–8, which is crucial for the practical application of these materials. Moreover, modifying the biochar surface with iron oxides significantly increases U(VI) removal efficiency, particularly due to its enhanced affinity for uranium anionic complexes.

Additionally, using palygorskite (attapulgite) as a clay raw material for such composites can have a positive effect. Since this mineral's particles are needle-shaped, this can improve the diffusion permeability of the composites [13].

Starch is a renewable and readily available raw material with high carbon content, making it promising for biochar production. During pyrolysis, starch can transform into a carbon material with a developed porous structure. Such biochars have proven to be effective adsorbents for removing heavy metal ions and other pollutants [14,15].

Therefore, developing new composite adsorbents based on biochar, palygorskite, and iron oxides is a promising direction for improving the efficiency of water treatment from heavy metals and radionuclides. This study aims to synthesize these composites, analyse their structure and physicochemical characteristics, and investigate their effectiveness in removing U(VI) from aqueous solutions.

Experimental

Materials

The study used palygorskite from the Cherkasy deposit, which was pre-purified from quartz impurities and other minerals. The determined cation exchange capacity (CEC) of palygorskite is 0.3 mmol/g. Potato starch (analytical grade) was used as the biochar source, and iron (III) chloride hexahydrate ($\text{FeCl}_3 \cdot 6\text{H}_2\text{O}$) was used as the iron oxide source. Uranyl sulphate trihydrate ($\text{UO}_2\text{SO}_4 \cdot 3\text{H}_2\text{O}$ analytical grade) was used to prepare U(VI) solutions of various concentrations. The pH of initial solutions was adjusted by adding HCl or NaOH solutions.

Methods

For sample synthesis, the following method was used. A solution of $\text{FeCl}_3 \cdot 6\text{H}_2\text{O}$ (400 mL, 0.1M) was combined with corresponding amounts of starch and palygorskite (Table 1). The resulting suspension was thoroughly mixed using a magnetic stirrer for 1 hour. Afterward, sodium hydroxide solution (0.2 M) was added dropwise to the suspension until reaching pH 8.5–9. The resulting precipitate was separated by filtration and washed several times with distilled water until the wash water reached a neutral pH (pH 7). The filtered precipitate was dried at 60°C and then subjected to pyrolysis in closed alumina crucibles with a heating rate of 10°C/min up to 600°C and held for an additional hour.

After heat treatment, the crucibles with samples were rapidly cooled to room temperature. The samples were ground and sieved to a fraction <0.2 mm. The obtained powdered composites were stored in airtight containers until further use.

Table 1

Composition of initial systems for sample synthesis.

Sample	Palygorskite, (g)	Starch, (g)	$V\ 0.1M$ $FeCl_3 \cdot 6H_2O$, (L)
1	0	30	
2	1	20	
3	3	12	0.4
4	5	4	
5	10	0	

The textural parameters of the composites were determined by low-temperature nitrogen adsorption using a NOVA-2200 station (Quantachrome, USA). The degassing temperature was 150°C at a pressure of 0.0134 Pa. The specific surface area (S_{BET}) of the samples was calculated using the Brunauer-Emmett-Teller (BET) method. Pore size distribution was obtained using density functional theory (DFT) (N_2 at 77 K on silica (cylindr. pore, NLDFT equilibrium model). Micropore volume was calculated using the Dubinin-Radushkevich model (DR). The total pore volume (V_t) was calculated at the maximum volume of adsorbed nitrogen at a relative pressure $p/p_0 = 0.99$. The values of the average pore radius (r_a) were also calculated.

Fourier transform infrared spectroscopy (ATR-FTIR) was acquired using a Vertex 70 spectrometer (Bruker, Germany) in attenuated total reflectance (ATR) mode in the wavenumber range of 4000–400 cm^{-1} , with a resolution of 4.0 cm^{-1} (number of scans: 64). The investigation utilised a single-reflection diamond ATR accessory (Platinum ATR, Bruker Optics GmbH).

X-ray phase analysis of the samples was performed using a SmartLab SE diffractometer (Rigaku, Japan). Diffraction patterns were recorded using $CuK\alpha$ radiation in continuous mode at a speed of 5°/min and with a step of 0.02°. The phase composition was determined using the Powder Diffraction File (PDF) database provided by the International Centre for Diffraction Data (ICDD).

Electron microscopy studies (SEM) were conducted using a JSM-6700F field emission scanning electron microscope (JEOL, Japan). Chemical (oxide composition) was determined for a series of points (1–15) using energy-dispersive X-ray spectroscopy (EDX).

U(VI) sorption. The sorption capacity of the composites for uranium(VI) removal was determined using a standard method. A 0.1 g of each sample was brought into contact with 50 cm^3 of uranium(VI) solution at the appropriate concentration and pH. To study the dependence of sorption capacity on initial solution pH, a uranium(VI) concentration of 100 $\mu mol/L$ was used. The previously determined time for establishing adsorption equilibrium was 240 minutes, based on preliminary kinetic experiments conducted with continuous mixing on an orbital shaker (Biosan ES-20) at 200 rpm and 25°C. These experiments were aimed at evaluating the contact time required for equilibrium and were used to define the duration of subsequent adsorption tests. While they confirmed that equilibrium was reached within 240 minutes for all studied samples, the data obtained were not sufficient for detailed kinetic modelling. Additional, more precise kinetic experiments are planned to clarify the adsorption mechanism and better characterise the adsorption kinetics. After reaching adsorption equilibrium, the liquid phase was separated by membrane filter 0.45 μm . The residual uranium(VI) content was determined spectrophotometrically using Arsenazo III reagent at a wavelength of 651 nm using a UNICO-UV 2100 spectrophotometer (United Products Instruments, USA). The experimental data were correlated by using the Langmuir and Freundlich models.

Results and discussion

Characterisation of the phase composition, texture and surface of composites

The X-ray phase analysis results (Figure 1) indicate the presence of several iron oxide phases. For samples 1–4, which contain the carbon component, the magnetite Fe_3O_4 phase (PDF #19-0629) is present, which requires reducing conditions for formation. In sample 5, which lacks starch in its initial composition, the formation of hematite Fe_2O_3 phase (PDF #33-0664) is observed.

The reflection at angle 35.5° can be characteristic of both hematite ($\alpha-Fe_2O_3$) and magnetite (Fe_3O_4), as their crystal structures have similar interplanar distances in this region. For magnetite ($d \approx 0.253$ nm) corresponds to angle at $2\theta \approx 35.5^\circ$. For hematite, the reflection $d \approx 0.252$ nm is located in the region at $2\theta \approx 35.6^\circ$. The permissible error of $\pm 0.2^\circ$ must also be taken into account.

All samples show the presence of sodium chloride phase (PDF #05-0628), which has a relatively high degree of crystallinity and pronounced reflections in the diffraction patterns (Figure 1).

Since complete removal of sodium chloride residues is hard to achieve, during sample drying and subsequent heat treatment, its concentration increases significantly and comprises a portion in the final product that becomes noticeable in the diffraction patterns.

Palygorskite typically has a relatively low degree of crystallinity, and its reflections in the diffraction patterns overlap with other phases. Additionally, the synthesis method produces samples with a high degree of homogenization, which inevitably leads to significant sample heterogeneity and consequently weak reflections in the diffraction patterns. Furthermore, as established [16], palygorskite begins to undergo phase transformations at temperatures above 300°C, and at 600°C, partial sintering occurs along with the formation of α -quartz, α -cristobalite, and magnesium silicate phases.

The texture of the composites significantly depends on the initial sample composition. According to IUPAC classification, the nitrogen sorption isotherms (Figure 2(a)) can be classified as Type IV. They show a distinct sigmoidal profile with an uptake at high p/p_0 values. This isotherm shape is characteristic of materials predominantly containing mesopores (2 to 50 nm). The sharp uptake in the final portion of the isotherm

(from 0.6 p/p_0) indicates the filling of large pores or particle agglomerates, as well as capillary condensation phenomena. The hysteresis loop shapes can be classified as Type H1 or H3, which is characteristic of materials containing tubular or wedge-shaped pores [17]. The pore size distribution according to the DFT model used is presented in Figure 2(b).

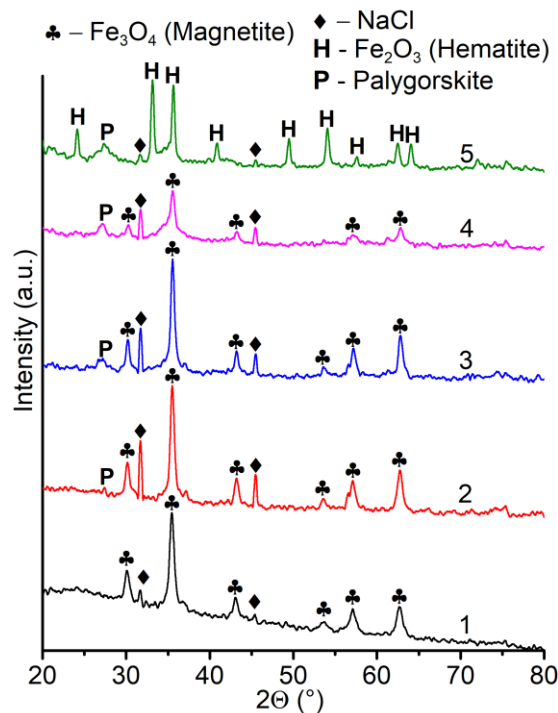


Figure 1. X-ray diffraction patterns of composite samples.

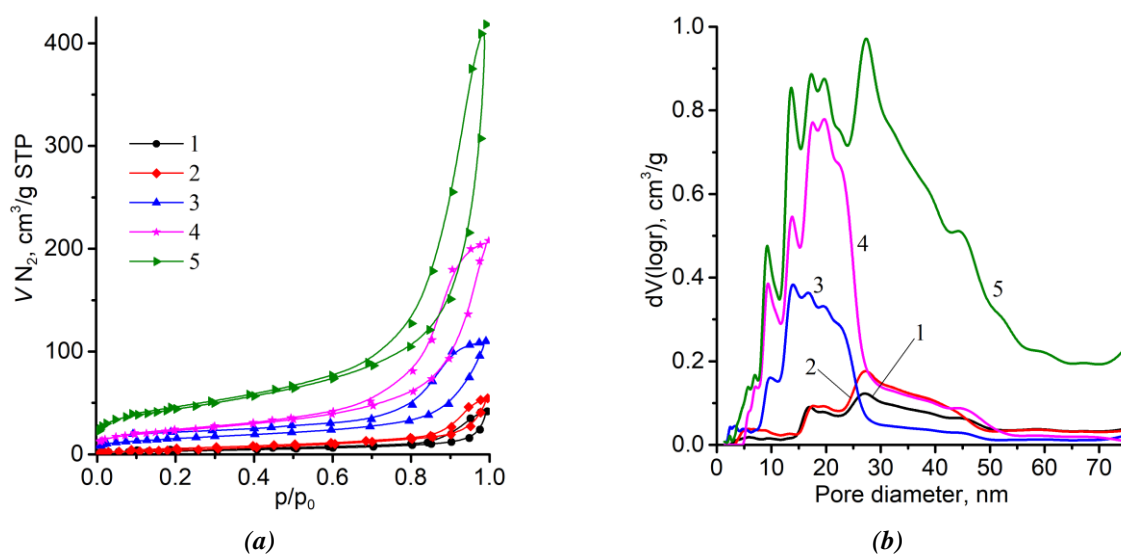


Figure 2. Textural parameters of the composites. Nitrogen adsorption isotherms of composite samples (a) and pore size distribution based on the DFT method (b).

Samples 1 and 2 have similar pore size distributions, with curves showing a similarity of curve profiles, which may be related to the low palygorskite content in these materials. For samples 3 and 4, a narrowing of the distribution is observed with a predominant pore diameter range from 10 to 30 nm. For sample 5, this distribution widens from 10 to 40 nm. The synthesized composite samples have optimal textural characteristics, as they contain predominantly mesopores, which is important for sorption processes. The presence of biochar and iron oxide phases likely provides the composites with mesoporosity and a relatively narrow pore size distribution, since these properties are not characteristic of palygorskites [18]. Furthermore, somewhat reduced specific surface area values for S_{BET} or S_{DFT} are observed, which is also related to the predominant presence of mesopores in the samples (Table 2).

The specific surface area of micropores according to the Dubinin-Radushkevich model ($S_{m\ DR}$) also indicates a gradual increase in micropore content with increasing palygorskite content, for which the specific surface area can reach 213 m²/g [19].

The IR spectra of the composite samples (Figure 3) indicate the presence of characteristic groups. Broad bands around 3600–3300 cm^{−1} likely correspond to O–H stretching vibrations, which are typically associated with hydroxyl groups (–OH) of biochar, on the surface of iron oxides, as well as with adsorbed water molecules on the samples [20]. Sample 5 shows higher transmittance in the 3600–3300 cm^{−1} region, which may indicate an increased content of hydroxyl groups or adsorbed water.

The bands at 2923 and 2851 cm^{−1} may correspond to C–H stretching vibrations, indicating the presence of residual organic matter or aliphatic residues in the biochar. A significant decrease in their intensity is observed in the transition from sample 1 with high carbon content to sample 5 with its absence.

For all studied samples, characteristic bands at 2339 and 2360 cm^{−1} correspond to adsorbed CO₂. The elevated carbon dioxide content can be explained by the developed specific surface

area and the presence of residual alkaline components on the surface, which effectively retain carbon dioxide both from the air and during sample synthesis when pyrolysis of the organic component - starch - occurred [21].

The band at 1718 cm^{−1}, associated with C=O stretching vibrations of carbonyl groups [22], gradually decreases in intensity from samples 1 to 4, which is related to the decreasing biochar content in the samples. Similar changes are observed for the absorption band at 1382 cm^{−1}, caused by the symmetric vibrational band of C–O carboxyl groups on the surface of biochar fragments [23]. The band at 1645–1600 cm^{−1} is likely due to a combination of carbonyl groups, adsorbed water, and aromatic structures formed during pyrolysis [24].

Bands around 1100–1000 cm^{−1} may correspond to Si–O–Si stretching vibrations, which are characteristic of palygorskite [25]. Peaks in the range of 700–500 cm^{−1} likely correspond to Fe–O vibrations associated with iron oxide phases [26].

Overall, the IR spectra show that the samples contain absorption bands characteristic of biochar, iron oxides, and palygorskite. Pyrolysis at 600°C led to the decomposition of starch into biochar. The palygorskite structure underwent minimal changes, as temperatures higher than 600°C are required for its sintering processes [13].

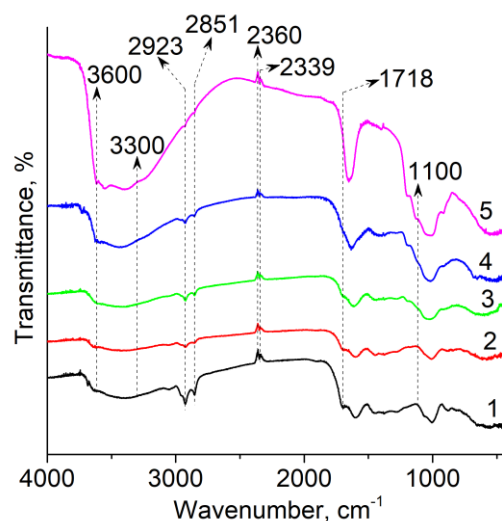


Figure 3. IR spectra of the composite samples.

Table 2

Textural properties of composites.					
Sample	S_{BET} (m ² /g)	S_{DFT} (m ² /g)	$S_{m\ DR}$ (m ² /g)	V_t (cm ³ /g)	r_a (nm)
1	13.1	13.5	12.6	0.06	9.85
2	19.9	18.7	18.2	0.08	8.47
3	54.7	60.2	61.5	0.17	6.21
4	82.8	81.4	87.3	0.32	7.75
5	155.6	151.3	179.2	0.65	8.31

The SEM images of the composite samples are presented in Figure 4. Samples 1 and 2 are characterised by the formation of a foam-like mass of carbon phase. This texture is formed by biochar with numerous pores and holes that mirror the shape and size of the original starch microgranules. According to literature data [27], the sizes of such granules typically range from 5 to 20 μm . This indicates the possibility of obtaining composites with a predetermined pore structure by selecting an appropriate type of carbon source.

For samples 3, 4, and 5, a change to a more amorphous texture is noted. These samples are characterised by significant inclusions of iron oxides, such as magnetite or hematite (for sample 5), which form due to thermal and chemical transformations during synthesis. These samples also show fragments of needle-like palygorskite particles or other phases that replicate the primary form of palygorskite particles. Sample 5 is characterized by a further increase in iron oxide content, confirmed by numerous particles with high contrast in backscattered electrons, typical for metallic and oxide phases. Additionally, structures appear that may correspond to products of partial phase transformations of palygorskite, indicating complex interactions between composite components during synthesis. It's worth noting that the texture of samples 1 and 2 reflects a high level of homogeneity in the carbon phase, while for

samples 3–5, the texture becomes more heterogeneous. This may be related to the formation of different mineral phases and their increased content in the composite structure. EDX analysis, with results shown in Table 3, demonstrates clear trends in the chemical composition changes from samples 1 to 5. Samples 1, 2, and 3 show high carbon content, related to starch decomposition during thermal treatment.

For example, in sample 1 (point number 1) the carbon content reaches 85.6%, indicating the dominant role of the carbon phase in the material structure. With decreasing starch amount in the initial pyrolysis mixture (4 g for sample 4 and no starch for sample 5), the carbon content gradually decreases, reaching practically zero values in samples 4 and 5.

The increase in palygorskite content significantly affects the chemical composition of the samples. Samples 4 and 5 show a significant increase in magnesium, aluminium, and silicon oxides content, which are components of palygorskite. Specifically, the SiO_2 content in samples 4 and 5 reaches 57.5 % (point 15), while Al_2O_3 and MgO content also increases significantly, reaching 11.6% and 8.2%, respectively. These changes indicate the dominance of the mineral phase in the composite structure, confirming the transition from carbon matrix to mineral matrix as the amount of starch decreases in the initial samples before pyrolysis.

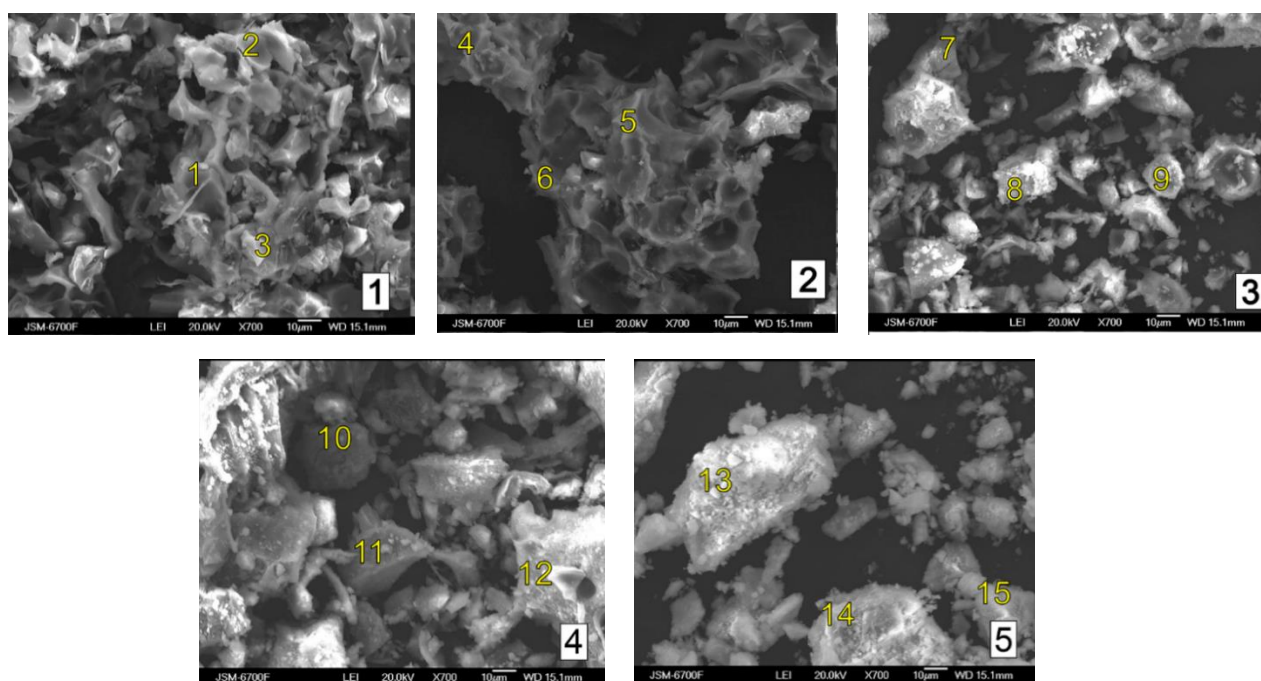


Figure 4. SEM micrographs of composite samples surfaces (sample numbers shown in white boxes and numbers 1-15 on the images indicate the EDX analysis points).

One characteristic feature of samples with palygorskite addition is the increased content of alkali metals - sodium and potassium. For example, the Na_2O content in samples 4 and 5 reaches 4.1% (point 11), and K_2O up to 0.6 %. This may be related both to the natural composition of palygorskite and to possible impurities present in the natural form of the mineral.

Iron oxides play an important role in the sample structure. Fe_xO_y in Table 3 means Fe_2O_3 or Fe_3O_4 or the mixture of both. In samples 1-3, their content varies between 13.7–94.8%, which is explained by the influence of initial components. In samples 4 and 5, the iron oxide content is also high (18.9–79.0%), confirming the formation of magnetite (Fe_3O_4) or hematite (Fe_2O_3) phases during pyrolysis.

The chloride content in all samples (for example, 3.4% at point 14 of sample 5) is residual and related to the use of reagents during iron hydroxide precipitation stages.

Sorption of uranium(VI)

Environmental contamination with uranium(VI) significantly depends on pH. The sorption efficiency of uranium from solutions with different pH levels was investigated (Figure 5(a)). A characteristic feature for uranium under these conditions is the complex extreme form of sorption dependence on the initial solution pH. This form is primarily related to the formation of various uranium(VI) coordination compounds along with parallel changes in the adsorbent surface charge depending on solution pH [28].

Table 3

Chemical composition of samples determined by EDX method.

Sample	Point number	C	Na_2O	K_2O	MgO	Al_2O_3	SiO_2	Cl	Fe_xO_y
1	1	85.6	0.7	–	–	–	–	–	13.7
	2	29.1	–	–	–	–	–	–	70.9
	3	41.5	–	–	–	–	–	–	57.8
	4	78.9	1.8	–	–	0.5	2.8	–	16.0
2	5	52.7	2.6	–	1.2	1.6	6.9	–	35.0
	6	40.2	1.5	–	–	–	0.9	–	57.4
	7	–	–	–	–	1.2	2.4	1.6	94.8
3	8	–	4.1	–	4.7	6.5	31.5	2.4	50.9
	9	56.7	10.4	–	1.8	2.1	8.1	7.2	13.8
	10	–	–	–	–	2.3	14.8	3.8	79.0
4	11	–	4.1	0.6	6.2	8.2	41.5	1.8	37.6
	12	–	3.9	–	3.0	4.6	22.2	2.8	63.5
	13	–	1.6	0.7	8.9	12.0	56.8	1.2	18.9
5	14	–	–	0.8	6.8	9.3	45.8	3.4	33.9
	15	–	–	1.0	8.2	11.6	57.5	1.9	19.8

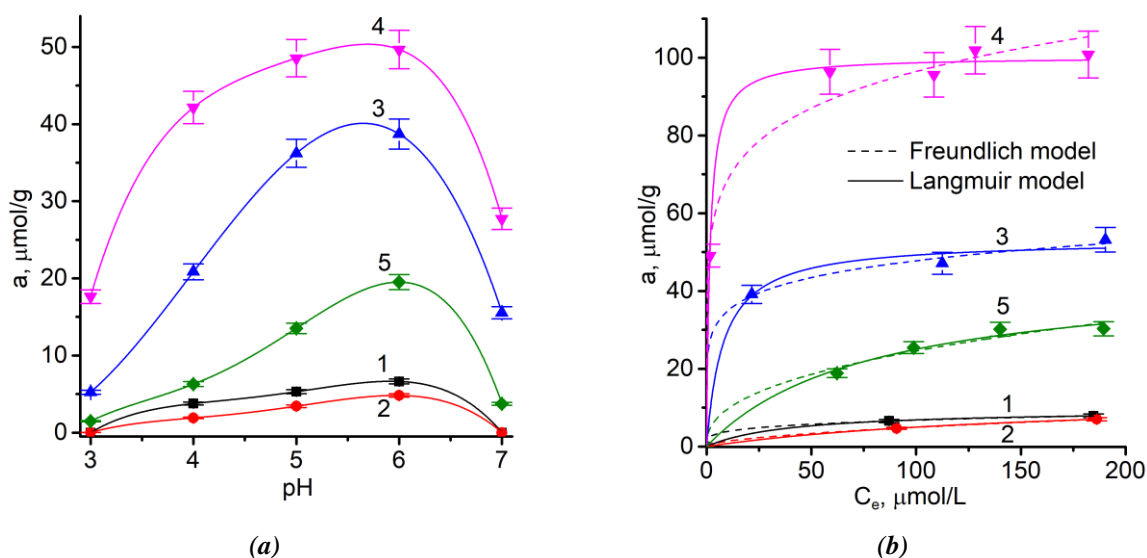


Figure 5. Uranium(VI) sorption behaviour. Uranium(VI) sorption as a function of pH of initial solutions (a) and uranium(VI) sorption isotherms for composite samples (b).

Table 4

Langmuir and Freundlich equation coefficients.						
Sample	Langmuir model			Freundlich model		
	K_L (L/ μ mol)	a_∞ (μ mol/g)	R^2	K_F (L/ μ mol)	n	R^2
1	0.025	9.6	0.9999	2.23	4.1	0.9992
2	0.006	13.2	0.9999	0.38	1.8	0.9993
3	0.125	53.2	0.9904	25.41	7.3	0.9972
4	0.632	100.2	0.9967	48.74	6.7	0.9871
5	0.013	44.4	0.9891	3.79	2.5	0.9803

In acidic media, uranium(VI) exists predominantly as uranyl cations (UO_2^{2+}) or sulphate complexes, which are poorly adsorbed on the protonated adsorbent surface. At pH 5.5–6 adsorption reaches its maximum, which is attributed to changes in the material's surface charge and the transition of uranium(VI) into polynuclear, multi-charged complexes with significantly higher sorption capacity. In alkaline media, negatively charged polynuclear hydroxo- and carbonate complexes predominate, which are weakly adsorbed on the negatively charged adsorbent surface.

Analysis of curves 1–5 indicates a significant influence of material composition on its sorption properties. Sample 1 shows higher sorption values than sample 2, which may be related to the exclusive presence of magnetite and biochar phases with residual carboxyl and other groups that have increased affinity for uranium(VI). In turn, sample 2 has lower sorption values than sample 1, despite having a higher specific surface area. This difference is likely related to the presence of palygorskite or differences between pyrolysis products, as confirmed by several studies [29,30]. The reduced sorption value for sample 2 may also be related to dilution, pore blocking, or the formation of less reactive phases when adding palygorskite. Additionally, pyrolysis under different conditions, including changes in pyrolysis atmosphere, significantly affects the hydrophilicity of biochar and its composite materials [31].

The sorption isotherms for the synthesized composites (Figure 5(b)) reveal significant variations in sorption properties with changes in the initial composition, with sorption capacities ranging from 10 to 100 μ mol/g. The application of Langmuir and Freundlich models allows for a comparative analysis of the sorption properties of the synthesized composites (Table 4).

For the samples, changes in the Langmuir adsorption equilibrium constant (K_L) are observed in the range from 0.006 to 0.63 L/ μ mol, indicating the level of affinity between adsorbate and adsorbent surface. The highest affinity is observed

for sample 4 with a K_L value of 0.63 L/ μ mol. The maximum adsorption capacity for sample 4 is also the highest at 100.2 μ mol/g. The correlation coefficients R^2 for the Langmuir model have higher values than for the Freundlich model, suggesting that the Langmuir model better describes the experimental data.

It's worth noting that sample 5 shows reduced values of maximum adsorption capacity a_∞ and equilibrium constant K_L , which is primarily related to the presence of iron oxides in the form of hematite rather than magnetite, as confirmed by X-ray phase analysis for samples 1–4. It's known that magnetite can have higher sorption properties for uranium(VI) than hematite, due to the ability of Fe^{2+} in magnetite composition to reduce uranium(VI) to insoluble uranium(IV), which precipitates on the sample surface [32].

Conclusions

The synthesized composites based on biochar, palygorskite, and iron oxides effectively remove uranium(VI) from aqueous solutions, with a maximum adsorption capacity of 100.2 μ mol/g, confirming the effectiveness of combining magnetite, palygorskite, and biochar phases along with a developed mesoporous structure. The Langmuir adsorption equilibrium constant for the best sample was 0.632 L/ μ mol, indicating high adsorbent affinity for uranium(VI).

The textural properties of the composites, particularly specific surface area and pore size distribution, significantly depend on the composition of initial systems. Samples with high biochar content have predominantly mesoporous structures with pores of 10–30 nm, which facilitates adsorption processes. On the other hand, the sample with high palygorskite content and no starch shows reduced adsorption capacity of 44.4 μ mol/g due to hematite phase formation.

The results confirm that pH 5.5–6 is optimal for uranium(VI) removal, where the adsorption capacity of synthesised materials reaches its maximum due to changes in adsorbent surface charge and the formation of multi-charged uranium complexes. The developed composites can be

considered as alternative adsorbents for water system purification, as they have stable adsorption characteristics and broad potential for practical application.

Acknowledgments

The authors express their gratitude to Dr. M.V. Borysenko, Senior Researcher at the Chuiko Institute of Surface Chemistry, National Academy of Sciences of Ukraine, for his assistance in obtaining and processing FTIR analysis.

References

1. Gao, N.; Huang, Z.; Liu, H.; Hou, J.; Liu, X. Advances on the toxicity of uranium to different organisms. *Chemosphere*, 2019, 237, 124548, pp. 1–13. DOI: <https://doi.org/10.1016/j.chemosphere.2019.124548>
2. Ighalo, J.O.; Chen, Z.; Ohoro, C.R.; Oniye, M.; Igwegbe, C.A.; Elimhngbovo, I.; Khongthaw, B.; Dulta, K.; Yap, P.-S.; Anastopoulos, I. A review of remediation technologies for uranium-contaminated water. *Chemosphere*, 2024, 352, 141322, pp. 1–21. DOI: <https://doi.org/10.1016/j.chemosphere.2024.141322>
3. Aly, M.M.; Hamza, M.F. A review: Studies on uranium removal using different techniques. Overview. *Journal of Dispersion Science and Technology*, 2013, 34(2), pp. 182–213. DOI: <https://doi.org/10.1080/01932691.2012.657954>
4. Fahad, S.A.; Nawab, M.S.; Shaida, M.A.; Verma, S.; Khan, M.U.; Siddiqui, V.; Naushad, M.; Saleem, L.; Farooqi, I.H. Carbon based adsorbents for the removal of U(VI) from aqueous medium: A state of the art review. *Journal of Water Process Engineering*, 2023, 52, 103458, pp. 1–35. DOI: <https://doi.org/10.1016/j.jwpe.2022.103458>
5. Yang, X.; Zhou, Y.; Hu, J.; Zheng, Q.; Zhao, Y.; Lv, G.; Liao, L. Clay minerals and clay-based materials for heavy metals pollution control. *Science of the Total Environment*, 2024, 954, 176193, pp. 1–22. DOI: <https://doi.org/10.1016/j.scitotenv.2024.176193>
6. Gupta, K.; Joshi, P.; Gusain, R.; Khatri, O.P. Recent advances in adsorptive removal of heavy metal and metalloid ions by metal oxide-based nanomaterials. *Coordination Chemistry Reviews*, 2021, 445, 214100, pp. 1–23. DOI: <https://doi.org/10.1016/j.ccr.2021.214100>
7. Li, M.; Liu, H.; Chen, T.; Dong, C.; Sun, Y. Synthesis of magnetic biochar composites for enhanced uranium(VI) adsorption. *Science of the Total Environment*, 2019, 651(1), pp. 1020–1028. DOI: <https://doi.org/10.1016/j.scitotenv.2018.09.259>
8. Liang, G.; Wang, Z.; Yang, X.; Qin, T.; Xie, X.; Zhao, J.; Li, S. Efficient removal of oxytetracycline from aqueous solution using magnetic montmorillonite-biochar composite prepared by one step pyrolysis. *Science of the Total Environment*, 2019, 695, 133800, pp. 1–12. DOI: <https://doi.org/10.1016/j.scitotenv.2019.133800>
9. Tang, J.; Mu, B.; Zong, L.; Wang, A. From waste hot-pot oil as carbon precursor to development of recyclable attapulgite/carbon composites for wastewater treatment. *Journal of Environmental Sciences*, 2018, 75, pp. 346–358. DOI: <https://doi.org/10.1016/j.jes.2018.05.014>
10. Arif, M.; Liu, G.; Yousaf, B.; Ahmed, R.; Irshad, S.; Ashraf, A.; Zia-Ur-Rehman, M.; Rashid, M.S. Synthesis, characteristics and mechanistic insight into the clays and clay minerals-biochar surface interactions for contaminants removal - A review. *Journal of Cleaner Production*, 2021, 310, 127548, pp. 1–16. DOI: <https://doi.org/10.1016/j.jclepro.2021.127548>
11. Sun, S.; Zeng, X.; Gao, Y.; Zhang, W.; Zhou, L.; Zeng, X.; Liu, W.; Jiang, Q.; Jiang, C.; Wang, S. Iron oxide loaded biochar/attapulgite composites derived *camellia oleifera* shells as a novel bio-adsorbent for highly efficient removal of Cr(VI). *Journal of Cleaner Production*, 2021, 317, 128412, pp. 1–10. DOI: <https://doi.org/10.1016/j.jclepro.2021.128412>
12. Rawal, A.; Joseph, S.D.; Hook, J.M.; Chia, C.H.; Munroe, P.R.; Donne, S.; Lin, Y.; Phelan, D.; Mitchell, D.R.G.; Pace, B.; Horvat, J.; Webber, J.B.W. Mineral–Biochar composites: molecular structure and porosity. *Environmental Science & Technology*, 2016, 50(14), pp. 7706–7714. DOI: <https://doi.org/10.1021/acs.est.6b00685>
13. Tian, L.; Wang, L.; Wang, K.; Zhang, Y.; Liang, J. The preparation and properties of porous sepiolite ceramics. *Scientific Reports*, 2019, 9, 7337, pp. 1–9. DOI: <https://doi.org/10.1038/s41598-019-43918-9>
14. Suo, F.; You, X.; Ma, Y.; Li, Y. Rapid removal of triazine pesticides by P doped biochar and the adsorption mechanism. *Chemosphere*, 2019, 235, pp. 918–925. DOI: <https://doi.org/10.1016/j.chemosphere.2019.06.158>
15. Li, Y.; Peng, L.; Li, W. Adsorption behaviors on trace Pb²⁺ from water of biochar adsorbents from konjac starch. *Adsorption Science & Technology*, 2020, 38(9–10), pp. 344–356. DOI: <https://doi.org/10.1177/0263617420948699>
16. Shi, T.; Liu, Y.; Zhang, Y.; Lan, Y.; Zhao, Q.; Zhao, Y.; Wang, H. Calcined attapulgite clay as supplementary cementing material: thermal treatment, hydration activity and mechanical properties. *International Journal of Concrete Structures and Materials*, 2022, 16, pp. 1–10. DOI: <https://doi.org/10.1186/s40069-022-00499-8>
17. Sing, K.S.W.; Rouquerol, F.; Rouquerol, J. Classical Interpretation of Physisorption Isotherms at the Gas–Solid Interface. Rouquerol, F.; Rouquerol, J.; Sing, K.S.W.; Llewellyn, P.; Maurin, G. Eds. *Adsorption by Powders and Porous Solids. Principles, Methodology and Applications*. Elsevier, 2012, pp. 159–189. DOI: <https://doi.org/10.1016/B978-0-08-097035-6.00005-X>

18. Huang, R.; Wu, L.; Wang, X.; Zhao, M.; Tian, W.; Tang, N.; Gao, L. Effect of isomorphic replacement of palygorskite on its heavy metal adsorption performance. *AIP Advances*, 2023, 13(8), 085218, pp. 1–12. DOI: <https://doi.org/10.1063/5.0159845>
19. Tobilko, V.; Spasonova, L.; Kovalchuk, I.; Kornilovych, B.; Kholodko, Y. Adsorption of Uranium (VI) from aqueous solutions by amino-functionalized clay minerals. *Colloids and Interfaces*, 2019, 3(1), 41, pp. 1–11. DOI: <https://doi.org/10.3390/colloids3010041>
20. De Araújo, T.P.; Quesada, H.B.; Bergamasco, R.; Vareschini, D.T.; De Barros, M.A.S.D. Activated hydrochar produced from brewer's spent grain and its application in the removal of acetaminophen. *Bioresource Technology*, 2020, 310, 123399, pp. 1–7. DOI: <https://doi.org/10.1016/j.biortech.2020.123399>
21. Geetha, T.; Smitha, J.K.; Sebastian, M.; Litty, M.I.; Joseph, B.; Joseph, J.; Nisha, T.S. Synthesis and characterization of nano iron oxide biochar composite for efficient removal of crystal violet from water. *Heliyon*, 2024, 10(21), e39450, pp. 1–15. DOI: <https://doi.org/10.1016/j.heliyon.2024.e39450>
22. Cai, Y.; Qi, H.; Liu, Y.; He, X. Sorption/Desorption behavior and mechanism of NH_4^+ by biochar as a nitrogen fertilizer sustained-release material. *Journal of Agricultural and Food Chemistry*, 2016, 64(24), pp. 4958–4964. DOI: <https://doi.org/10.1021/acs.jafc.6b00109>
23. Kong Yong, S.; Leyom, J.; Chay Tay, C.; Abdul Talib, S. Sorption of lead from aqueous system using cocoa pod husk biochar: kinetic and isotherm studies. *International Journal of Engineering and Technology*, 2018, 7(3.11), pp. 241–244. DOI: <https://doi.org/10.14419/ijet.v7i3.11.16017>
24. Rallet, D.; Paltah, A.; Tsamo, C.; Loura, B. Synthesis of clay-biochar composite for glyphosate removal from aqueous solution. *Heliyon*, 2022, 8(3), e09112, pp. 1–8. DOI: <https://doi.org/10.1016/j.heliyon.2022.e09112>
25. Madejová, J.; Komadel, P. Baseline studies of the clay minerals society source clays: infrared methods. *Clays and Clay Minerals*, 2001, 49(5), pp. 410–432. DOI: <https://doi.org/10.1346/ccmn.2001.0490508>
26. Chen, T.; Wen, X.; Li, X.; He, J.; Yan, B.; Fang, Z.; Zhao, L.; Liu, Z.; Han, L. Single/co-adsorption and mechanism of methylene blue and lead by β -cyclodextrin modified magnetic alginate/biochar. *Bioresource Technology*, 2023, 381, 129130, pp. 1–8. DOI: <https://doi.org/10.1016/j.biortech.2023.129130>
27. Wang, C.; Tang, C.H.; Fu, X.; Huang, Q.; Zhang, B. Granular size of potato starch affects structural properties, octenylsuccinic anhydride modification and flowability. *Food Chemistry*, 2016, 212, pp. 453–459. DOI: <https://doi.org/10.1016/j.foodchem.2016.06.006>
28. Pylypenko, I.; Kovalchuk, I.; Tsyba, M. Development of granular composites based on laponite and Zr/Fe-alginate for effective removal of uranium (VI) from sulfate solutions. *Eastern-European Journal of Enterprise Technologies*, 2023, 6(10), 126, pp. 27–34. DOI: <https://doi.org/10.15587/1729-4061.2023.292524>
29. Albis, A.R.A.; Munoz, E.O.; Ariza, I.P.; Escobar, A.F.S.; Barraza, C.S.A. TG characterization of pyrolysis of cassava starch residues catalyzed by ferric sulfate. *Contemporary Engineering Sciences*, 2018, 11(72), pp. 3587–3597. DOI: <https://doi.org/10.12988/ces.2018.87365>
30. Xia, S.; Yang, H.; Lei, S.; Lu, W.; Cai, N.; Xiao, H.; Chen, Y.; Chen, H. Iron salt catalytic pyrolysis of biomass: Influence of iron salt type. *Energy*, 2023, 262(A), 125415, pp. 1–8. DOI: <https://doi.org/10.1016/j.energy.2022.125415>
31. Yang, L.; Jin, X.; Chen, Z. Intrinsic structure-function connections of carbon-encapsulated nanoscale zero-valent-iron using various pyrolysis atmospheres. *Journal of Environmental Management*, 2025, 373, 123768, pp. 1–9. DOI: <https://doi.org/10.1016/j.jenvman.2024.123768>
32. Ma, Y.; Cheng, X.; Kang, M.; Yang, G.; Yin, M.; Wang, J.; Gang, S. Factors influencing the reduction of U(VI) by magnetite. *Chemosphere*, 2020, 254, 126855, pp. 1–9. DOI: <https://doi.org/10.1016/j.chemosphere.2020.126855>